applied sciences

MDPI

Article

Baseline Subsoil CO_2 Gas Measurements and Micrometeorological Monitoring: Above Canopy Turbulence Effects on the Subsoil CO_2 Dynamics in Temperate Deciduous Forest

Didi Adisaputro [1,2,3,*], Philippe De Donato [1], Laurent Saint-Andre [2], Odile Barres [1], Catherine Galy [4], Gilles Nourrisson [2], Médéric Piedevache [5] and Marion Derrien [5]

1 GeoRessources Laboratory, Université de Lorraine, CNRS, BP 70239, 54506 Vandœuvre-lès-Nancy, France; Philippe.De-Donato@univ-lorraine.fr (P.D.D.); Odile.Barres@univ-lorraine.fr (O.B.)
2 INRAE, UR BEF, Centre de Nancy, 54280 Champenoux, France; Laurent.Saint-Andre@inrae.fr (L.S.-A.); gilles.nourrisson@inrae.fr (G.N.)
3 Institut Teknologi Sumatera, Way Huwi 35365, Lampung, Indonesia
4 ANDRA, 55290 Bure, France; Catherine.GALY@andra.fr
5 Solexperts France, 17 av de la Forêt de Haye, 54500 Vandoeuvre lès Nancy, France; Mederic.Piedevache@solexperts.fr (M.P.); Marion.Derrien@solexperts.fr (M.D.)
* Correspondence: Didi.adisaputro@univ-lorraine.fr

Citation: Adisaputro, D.; De Donato, P.; Saint-Andre, L.; Barres, O.; Galy, C.; Nourrisson, G.; Piedevache, M.; Derrien, M. Baseline Subsoil CO_2 Gas Measurements and Micrometeorological Monitoring: Above Canopy Turbulence Effects on the Subsoil CO_2 Dynamics in Temperate Deciduous Forest. *Appl. Sci.* **2021**, *11*, 1753. https://doi.org/10.3390/app11041753

Academic Editor: Stefan Fleck
Received: 17 January 2021
Accepted: 8 February 2021
Published: 18 February 2021

Featured Application: This work emphasizes the importance of the deep soil zone and above groundwater that can be applied to create a CO_2 baseline for a wide range of geological storage applications.

Abstract: Accurate and continuous measurement of the subsoil CO_2 is critical to better understand the terrestrial and atmosphere gas transfer process. This work aims to develop and field test a specific flow system to continuously measure the soil gas concentration (χc) and understand its main physical drivers. Hourly data measured in situ were collected through two dedicated wells at 1 m and 6 m depth coupled with micrometeorological measurement. Our study shows that χc at -1 m was at the lowest in winter and highest in summer. Meanwhile, the seasonal variation of χc at -6 m is somewhat unclear. While it is inevitable that temperature plays a significant role, this factor related to biological activity cannot fully explain the variation. The decrease in χc at both depths in summer coincides with an increase of friction velocity, especially during dry periods with R^2 of 0.68, which shows strong empirical evidence that wind turbulence plays a significant role in driving the deep soil CO_2. A monitoring strategy for gas measurement combining borehole and micrometeorological measurement offers excellent long-term monitoring possibilities to derive the vertical distribution of CO_2 and better understand the main physical drivers of gas exchange.

Keywords: subsoil gases; baseline monitoring; Forest; carbon dioxide; methane

1. Introduction

The gas exchange between the atmosphere and terrestrial ecosystem represents a large proportion of CO_2 and CH_4 atmospheric budgets [1]. Soil CO_2 budget and efflux due to land-use change averaged globally from 2009–2018 were estimated at 5496–8793.6 $PgCO_2$ and 5.49 $PgCO_2yr^{-1}$ respectively [2], as for the comparison, the emission due to fossil fuel combustion and the cement industry is around 33.4 $PgCO_2yr^{-1}$ [3]. Adequate and trustworthy monitoring strategies of natural gas exchange will help understand the local variability of gas concentration in the soil, e.g., in anticipation of the CO_2 injection [4,5] and promote public acceptability [6], or for ecological studies on terrestrial greenhouse gases emissions [3,7–9]. Generally, GHG (Greenhouse gasses) emissions from the soils

are being measured in both laboratories and directly in the field [3]. The most widely used approaches in this context are chambers methods (soil-air interface) [1,10–12], micrometeorological eddy covariance method (vegetation-atmosphere interface) [9,13–15], and the gradient method (subsoil gas transport) [1,12,16–19].

The monitoring of sub-soil CO_2 significantly helps define the overall balance between soil production and GHG consumption [20]. This soil CO_2 monitoring is also useful for comparing the carbon exchange quantification at the ecosystem level resulting from the flux tower [9,21,22]. It is widely believed that the soil CO_2 concentration generally increases as the depth, from the near-atmospheric layer up to a few meters below the topsoil. The CO_2 concentration below 20 cm for most soil types is between 0.2 and 4% [23]. Meanwhile, the CO_2 concentration above 10% is generally found in the active geothermal area with a significant pressure gradient transport instead of the solely diffusive process [24,25]. Although molecular diffusion plays a significant part in soil CO_2 emission, the physical components such as soil ventilation in highly porous surface layers, known as advective CO_2 transport involving wind speed, friction velocity (u*), or air pressure, are also important [26]. Friction velocity is a crucial parameter in the study of boundary layers. It can be described as $u^{*2} = \tau/\rho$, where ρ is the fluid density and τ is the shear stress. Friction velocity in a turbulent flow in the atmosphere is approximately constant up to the lowest several meters [27,28]. Nonetheless, multiple velocimeters that are positioned precisely are required in order to estimate the friction velocity. As alternatives, inertial dissipation, turbulent kinetic energy method, and eddy correlation method might be employed to produce reliable estimation [29].

The porous soil structure is continuously changing due to numerous factors, including water gains and losses, soil redistribution, changes in matrix structure because of the earthworms, and deformation due to compaction [30]. Some studies reported that the CO_2 dissolution and ventilation process plays a significant role in storing and releasing a large amount of CO_2 in subsurface cracks, pores, and cavities [31–33]. Nonetheless, most of the studies carried on forest soil mainly focused at a depth of 0 to 1 m, where the soil CO_2 production occurs from an autotrophic component and heterotrophic components. The deep soil zone, marginally influenced by the atmospheric conditions, is a perfect location to create a CO_2 baseline for a wide range of geological storage applications, including but not limited to the CCS (carbon capture and storage) [6,34,35] and hydrogen storage monitoring programs [36]. However, there was substantial evidence from previous works that soil gas transport in the unsaturated zone was predominantly affected by the water table variations. A study focusing on the monitoring and modeling aspects in the CCS Total pilot plant on Lacq-Rousse, France, shows that the soil CO_2 concentration was negatively correlated with changes in the piezometric level [37]. Specifically, the fluctuation is caused by the CO_2 dissolution or release process by the perched water table acting as a pump. There was also a strong indication of the seasonal condition affecting the variability of the CO_2 concentration in the soil [37]. Variation of subterranean CO_2 within the depth of 1.5 m was predominantly caused by pressure variations instead of biological or wind influences [38]. However, it is still uncertain whether these relationships exist in temperate forest ecosystems, which plays a significant role in carbon exchange through the biological cycle. The temperate forest ecosystem is also widely known as biologically active, storing a large quantity of soil organic carbon and a deep root system.

However, such studies cannot be conducted solely in the laboratory because the natural soil profile mostly consists of active Rhizophora-producing and consuming methane, plant-soil interactions, and spatial interaction [32]. The monitoring should be performed in long-term continuous monitoring with short hourly intervals to construct a reliable baseline of natural gas exchange, study its transport and production, and to better understand the influence of short-term events [6]. However, this approach has been considered economically unfeasible and complex. Therefore, there is a strong need to develop an economical and robust continuous soil gas measurement that requires low energy input and does not need complex maintenance. It can be complemented by automatic data transfer.

Measurement of the gas concentration using the low-resolution FTIR (Fourier-transform infrared spectroscopy) requires a calibration procedure by characterizing all of the spectrophotometer's instrumental line shape [39]. The chemical functional groups that absorb fundamental bands located at 2350 cm^{-1} for CO_2 and a combination of 1400–1200 cm^{-1} and 3200–2800 cm^{-1} for CH_4 can be used to quantify their concentration. FTIR technique takes into account the fact that the majority of the molecules absorb IR radiation, and the degree of the absorption is proportional to the concentration of the molecule. There are some significant conveniences in using FTIR including, (i) few optical elements; (ii) no need slits to attenuate radiation; (iii) outstanding stability and sensitivity (iv) high-speed data collection. FTIR also offers various benefits, such as near real-time operation, low maintenance, low cost, and simple structural specification [40,41]. Nonetheless, in term of its operation, FTIR spectroscopy has some limitations as follows: (i) This spectrometry can only be used for heteronuclear gases; (ii) it is considered as low resolution (1 cm^{-1}) that requires specific laboratory calibration for every single gas; (iii) it is superimposed by the presence of impurities [5,42], (iv) its implementation on long-time span in the field is difficult due to the required energy power.

The main objectives of this study are three-fold; (i) To develop and field test a specific flow system equipped with a membrane probe to continuously measure the soil gas concentration and auxiliaries data; (ii) to combine borehole with micrometeorological monitoring; (iii) to understand the main physical drivers of gas exchange in a deep soil layer (−6 m) and a shallow soil layer (−1 m) regardless of the water saturation conditions. In this paper, both the gas calibration procedure in the laboratory are described, and the observational setup of the measurement campaign, aspects of the data analysis, and analysis of the recorded time series of soil CO_2 and CH_4 concentration are shown.

2. Materials and Methods

2.1. Gas Analyzer

IN-SITU IR: Infrared spectra of gases were recorded in-situ using a portable infrared spectrometer ALPHA provided by BRUKER (Bruker Optik GmbH, Ettlingen, Germany) with high humidity optics and zinc selenide (ZnSe) beamsplitter. The spectra were acquired with 16 scans in the mid-infrared range (5000–600 cm^{-1}) with a spectral resolution of 4 and 1 cm^{-1} and a zero-filling factor of 2. A stainless-steel gas cell with a short path length (5 cm) with ZnSe windows was placed in the sampling module. The low-power NDIR sensor (home-made engineered) without moving part allows the continuous monitoring of solely CO_2 was also employed. In situ samples were also analyzed with a gas chromatography analyzer (CP-4900 Micro-Gc, Varian BV, Netherlands) to determine the soil gas composition, mainly CO_2 and CH_4. A more detailed explanation regarding the calibration technique of the primary gas analyzer (FTIR) is given below.

EX-SITU FTIR: Because of the low resolution used (1 cm^{-1}) for IR measurements, calibration curves for CO_2 and CH_4 analyses must be determined in the laboratory [43]. Two reference gases (CO_2: 99.7% ± 2% and 5000 ppm ± 5%) were used to create a CO_2 calibration curve, and one reference gas (CH_4: 5000 ppm ± 5%) was used to develop a CH_4 calibration curve. Furthermore, the reference gases were mixed using AlyTech GasMix™, an on-site customized gas standard preparation system with a relative uncertainty of less than 2% for various mixtures such as CO_2 and Ar, CO_2 and N_2, CH_4 and Ar, and CH_4 and N_2. The gas mix instrument is based on mixing, diluting, and injecting up to 12 gas standards at different concentrations that can be used for instrument calibration purposes. The gas standard was controlled in the software interface allowing the user to define the gas concentration, flow rate, and pressure. A G2201-I gas analyzer (Picarro Inc., Santa Clara, CA, USA) based on Cavity Ring-down Spectroscopy (CRDS) was used to verify the concentration indicated by the gas mix coupled with Gas Chromatography.

During the calibration procedure, the gas pressure inside the cell was measured using a built-in piezoresistive-based pressure gauge manufactured by Keller, ranging from 1 mbar to 1 kbar with an accuracy of 0.01–1%. A Pfeiffer vacuum model MVP 015-2 was

used during the measurement of references. The calibration was conducted at a constant room temperature of 22 °C and pressure of 1 ± 0.002 bar considering the total pressure most likely encountered ranges from 0.950 to 1.050 bar. Besides, the gas's temperature in the borehole is relatively stable, especially at −6 m, which was around 10 °C. The leak testing was carried out where this configuration managed to maintain its pressure of 0.02 bar within 15 min of the timeframe. The subtraction of atmospheric CO_2 was done for each recorded infrared spectrum to eliminate the ambient air background spectrum. The different spectral areas of CO_2 and CH_4 were calculated, as shown in Figure 1. As for the CO_2 concentration, the analysis is performed using the fundamental band located at 2350 cm^{-1} (ν_3) [2400; 2220] and for CH_4 using the fundamental bands at 1400–1200 cm^{-1} (ν_4) and 3200–2800 cm^{-1} (ν_3).

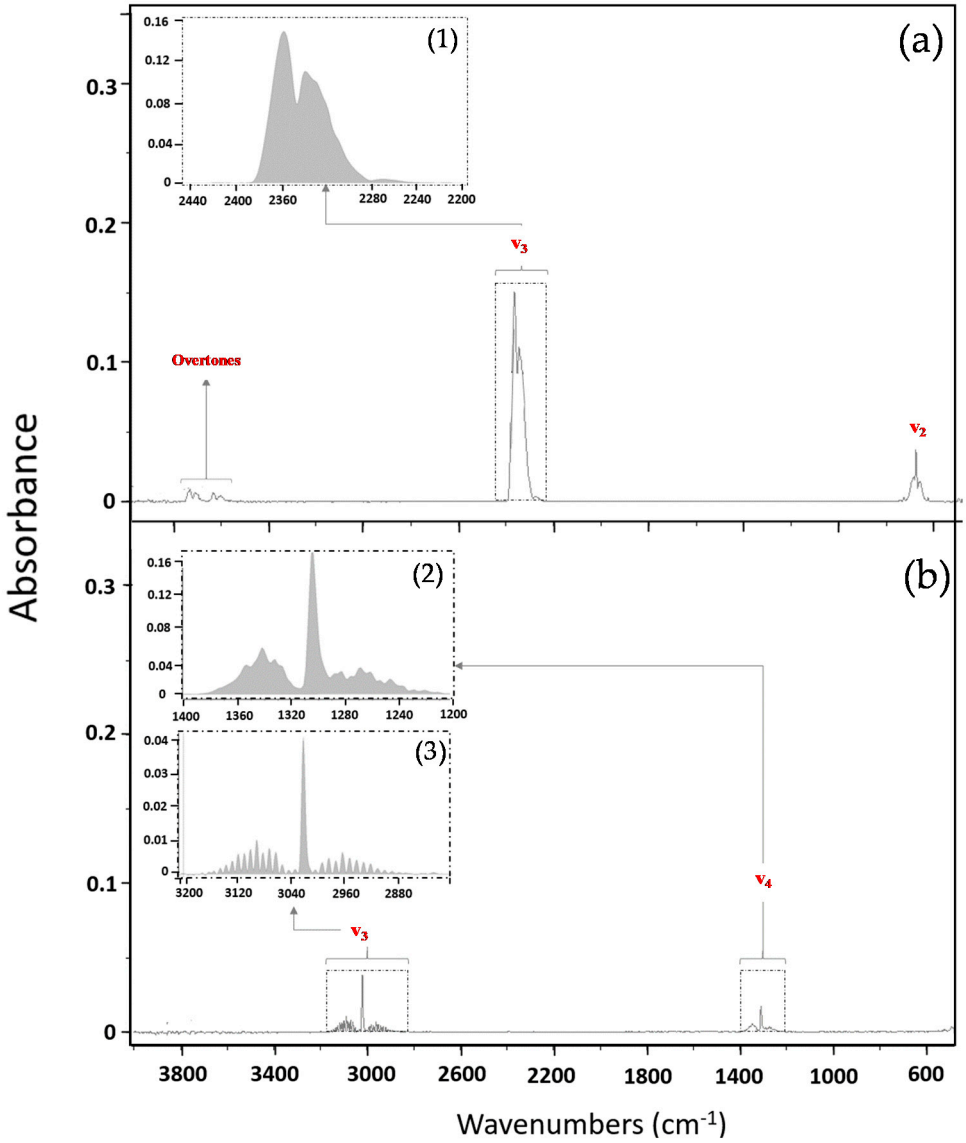

Figure 1. Infrared spectra of 3000 ppm of CO_2 (**a**) and 1800 ppm of CH_4 (**b**). For CO_2: frequency range for v3 area calculation (1). For CH_4: frequency range for v4 area calculation (2) and frequency range for v3 area calculation (3).

2.2. On-Field Implementation

The gas measurement was performed in the boreholes dedicated to investigating soil-gas concentration in the unsaturated zone with two depths of 1 m and 6 m. Those boreholes were drilled in June 2019 using a geotechnical rig capable of performing rotary

drilling. A borehole consists of a perforated pipe and a permanent well that was fitted with drilling tubes. Figure 2 shows the subsoil measurement system composed of three main parts, including completion (A), gas circulation module (B), and calibrated FTIR Bruker Alpha (C), with an additional GC analysis for cross-validating purpose. This well is dedicated to recording the gas phase's geochemical properties in the subsoil, which operates continuously and simultaneously equipped with a logs data station. The configuration of the subsoil measurement system was subject to previous research [5,37].

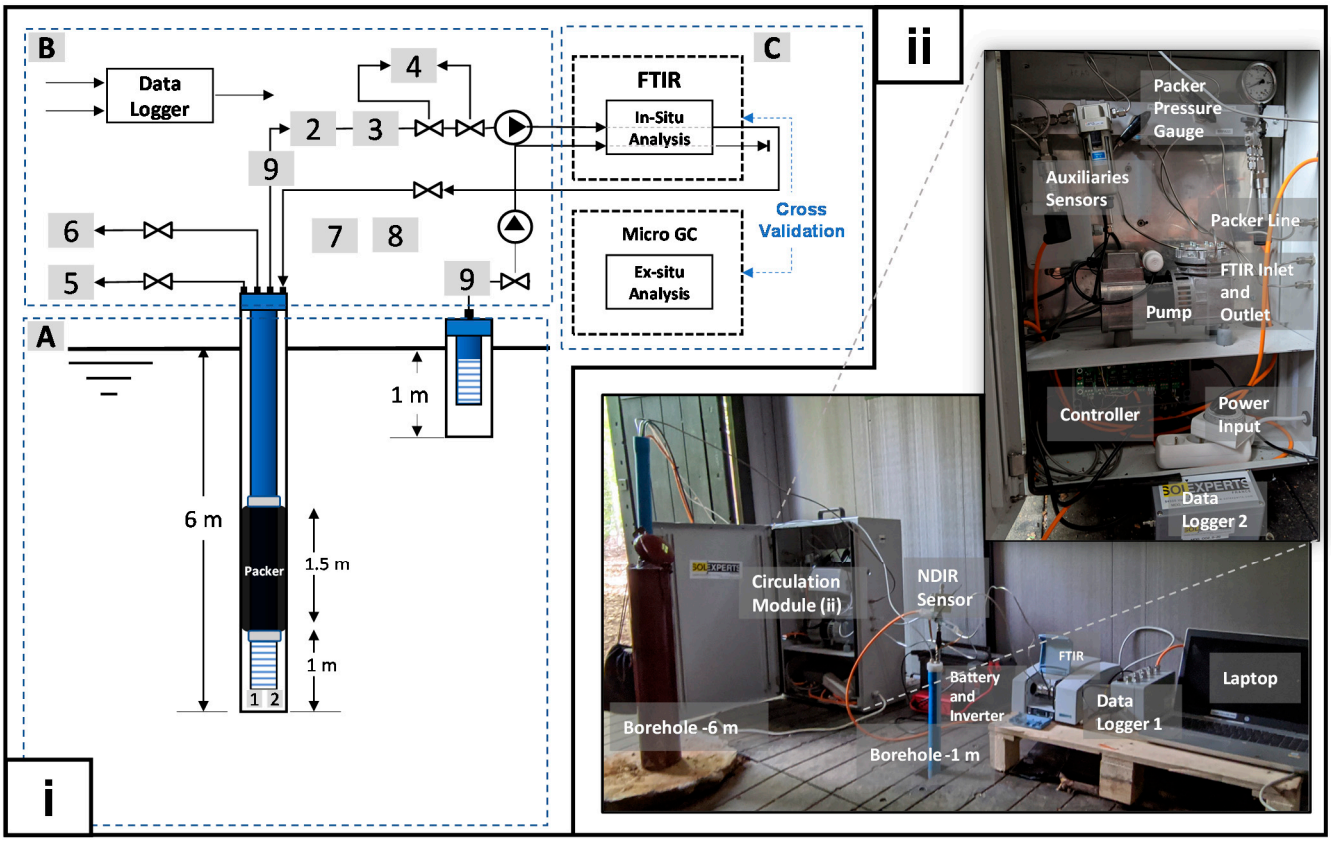

Figure 2. Monitoring concept for simultaneous and continuous gas measurement, including schematic diagram (i) and realistic view (ii) of monitoring infrastructure. The schematic diagram describes in more detail the process flow, which includes completion/boreholes (**A**), the circulation module (**B**), and calibrated FTIR Bruker Alpha with an additional GC sensor (**C**) for cross-validating. The circulation module consists of (1) temperature sensor, (2) pressure sensor, (3) water trap, (4) fluxmeter, (5) packer pressure, (6) borehole temperature indicator, (7) atmospheric temperature sensor, (8) atmospheric pressure sensor, (9) CO_2 NDIR sensor, and (10) soil moisture sensor.

The soil gases monitoring equipment (A) consists of three significant subparts: chamber, packer, and circulation lines. The collection chamber is an essential component that allows continuous sampling of the gas in the soil using an electric pumping system and a manual sampling port. The length and the diameter of the collection chamber is 60 cm and 50 mm, respectively. The packer made of an annular inflatable device of 64 mm long prevents any interferences with the ambient atmospheric gases by fully isolating the collection chamber. The circulation module consists of two lines of stainless steel, which is 4 mm in diameter allowing the gas to be transferred to the sensor and reintroduced into the borehole. The other two lines are equipped with pressure and temperature sensor. The gas flow module permits the gas sample's transportation from the sensor's completion and controls all parameters associated with the fluid flow (pressure, temperature, and flow). The gas circulation module (Figure 2B) was installed equipped with (a) circulation pump with a flow rate of 20 mL/min allowing the extraction and reintroduction of the gas in the collection chamber; (b) a water trap ensuring the control of the potentially liquid water in

the circuit by trapping the water and redirect its flow; (c) the flow meter and a pressure sensor measuring the flow rate and the pressure of the gas sample inside of the circulation module; (d) sample cells connected in parallel to the gas circuit allowing samples of gas for laboratory analysis without causing the ambient atmospheric gases to enter the system; (e) various types and sizes of valves; and (f) an inlet and an outlet to FTIR Bruker Alpha. Since the monitoring site had no access to grid power, three batteries with a total capacity of 300 Ah were used to supply the monitoring system's power.

2.3. Field Test

The subsoil gas was collected using a collection chamber via the pump at the rate of 20 mL/min. It operated for 10 min every hour to allow well-mixed gas in the system and conserve energy consumption. The gas passed through the temperature, pressure, and NDIR sensor before it was analyzed hourly through the IR gas cell and re-injected to the borehole's collection chamber. For every follow-up visit for replacing the battery, some gas samples were also collected to be cross-validated with gas chromatography. Subsoil gas spectra were recorded using FTIR for 16 scans over the range of 5000 to 600 cm^{-1} with a spectral resolution of 1 cm^{-1}. The Opus software allows integrating the various processing, including a continuous record of the spectra, eliminating the H_2O fingerprints, and calculating CO_2 concentration. Even though the water condensation can occur inside the gas circuit, it only interferes strongly with the combination band of 3609 cm^{-1} (Figure 1). Therefore, an additional correction is unnecessary since it does not interfere with the fundamental vibrational mode of CO_2 at 2400 cm^{-1}. In addition, the data collected and recorded are automatically uploaded and synchronized to the online platform of Mission OS once the Internet network is available. The obtained field data were further processed using open-source statistical computing and graphics software [44].

2.4. Site Description and Additional Recorded Data

The study was conducted at the beech forest described extensively in previous work [45]. This site was chosen due to some main criteria, including a high diversity of soil sequence, well-managed beech trees, homogeneous (species, age, and stem density), and having a minimum influence of the past forest management practices. The three studied soils' physicochemical properties have also been previously studied [45,46]. The dystric cambisol lies on the valanginian layer to around 200 cm of the depth with a pHw of 4.9 at the surface and 5.1 at a depth of 45–60 cm. The cationic exchange capacity (CEC) ranged from 0.9–6.7 cmolc kg^{-1} up to a depth of 60 cm of the vertical section. Sandy and clayey passages were found in the lower soil layer indicating the textural and structural heterogeneity caused by the complex sedimentary source material. A flux tower, 355 m apart from the boreholes (Figure 3), was used to record air temperature (T_{air}) using sensors installed at six different levels (HMP155, Vaisala, Vantaa, Finland), friction velocity (u*), soil water content (SWC) and soil surface temperature (T_{soil}), and precipitation (P). It was built at the end of 2012 in the framework of the ICOS (integrated carbon observation system) and as part of the Andra's long-term observatories (Ope). The tower reaches 45 m height above the ground. It allows the continuous measurement of the wind's speed, direction, and friction velocity (u*) at 35 m elevation (around 10m above forest canopy) using six 3D sonic anemometers (HS-50 Gill, Hampshire, UK) with a sampling rate of 10 Hz, and data were compiled per 30 min interval.

In this site, the wind direction is dominated by South and Southwest directions. The annual time series of environmental drivers and atmospheric χc (35 m) in 2018 showed that the monthly mean χc is highest in March with 431 ppm and the lowest in June at 401 ppm. The pattern across the soil temperature, air temperature, and net radiation unsurprisingly follows a seasonal pattern with the highest in July and the lowest in February with the range of the monthly average of 2.2 °C to 17.7 °C, −1.1 °C to 21.6 °C, 8.21 wm^{-2} to 665.8 wm^{-2} Respectively. Also, the precipitation is found to be intense in January, May, August, and December.

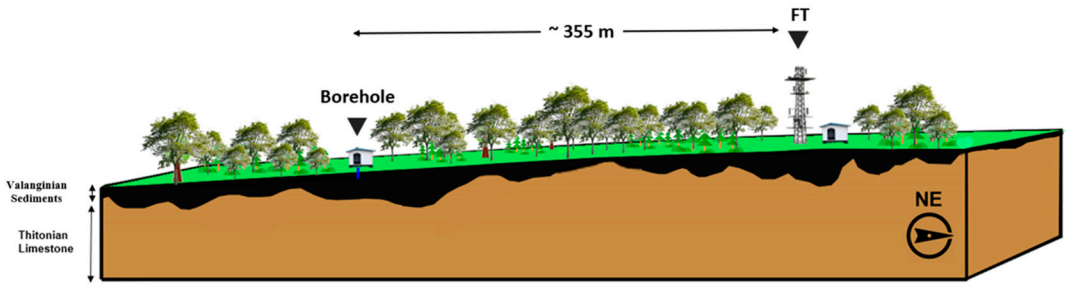

Figure 3. A vertical section of the soil profile of Tithonian limestone surmounted by valanginian sediments. On the surface, borehole measurement and a lattice tower (FT) were constructed with the distance around 355 m.

3. Results

3.1. Laboratory Calibration Results

The calibration curve of CO_2 and CH_4 was established in the laboratory after calculating the areas of the selected IR bands of CO_2 and CH_4, as presented in Figure 1. The calibration procedure consists of 11 measurement points for CO_2 (Figure 4a) and 13 measurement points for CH_4 (Figure 4b), on which the measurements were repeated three times with new references IR absorption spectrum for each point. The reference gas concentrations have also been cross-validated using the Picarro CRDS G2201-i analyzer and gas chromatography.

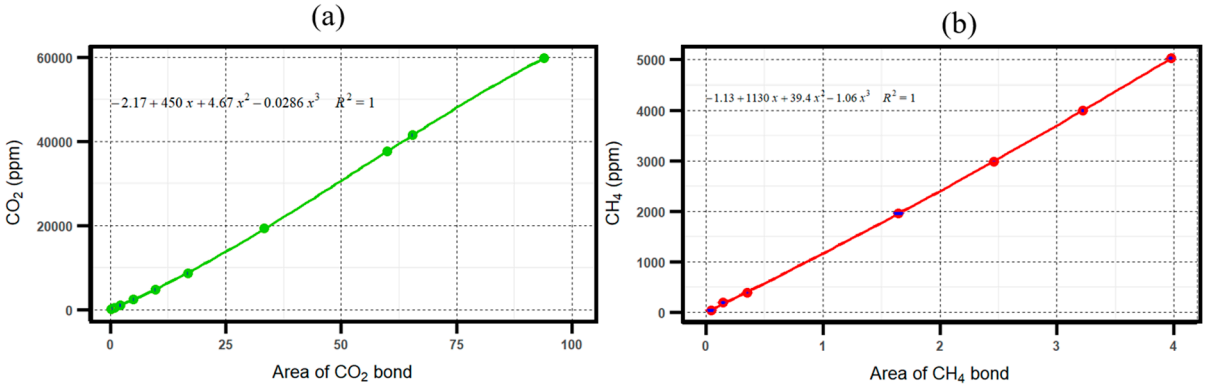

Figure 4. The calibration curve of CO_2 (**a**) shows a polynomial fitting of the CO_2 calibration curve on FTIR ranging from 101 ppm to 59,806 ppm. As for the CH_4 (**b**), the highest concentration that was applied was 5000 ± 99 ppm, with an average absorbance area (Abs) of 3.97 ± 0.012. The lowest concentration tested was 50 ppm, with an average absorbance area of 0.046 ± 0.024 (resolution: 1 cm^{-1}).

The lowest concentration of the standard gas tested is 101 ppm with an absorbance area (Abs) of 0.22. In comparison, the highest concentration tested is around 59,806 ppm, with an average absorbance area (Abs) of 94, As shown in Figure 1. In Table 1, the CO_2 concentration and the unit area have a large goodness fit of linear correlation with R^2 of 1 and a Y-intercept of −21.7 ppm. It also has a significant deviation from zero and a *p*-value of less than 0.0001. The CH_4 concentrations (50 to 5000) and the associated absorbance area have a large goodness fit of linear correlation with adjusted R^2 of 0.9999 and residual standard error of 32.14 ppm. It also has a significant deviation from zero and a *p*-value of less than 0.0001.

Table 1. The residual error and the adjusted R^2 of the two polynomial model fitting of CO_2 and CH_4 (Resolution: 1 cm^{-1}).

	Residuals by Section (ppm)					Residual Standard Error (ppm)	Adjusted R^2
CO_2 (100 to 60,000 ppm)	Min	1Q	Median	3Q	Max	57.84 on 15 degrees of freedom	1
	−81.94	−18.07	−3.33	7.58	109.58		
	Residual Standard Error (ppm)						
CH_4 (50 to 5000 ppm)	1	2	3	4	5	17.62 on 3 degrees of freedom	0.9999
	−5.97	21.23	−19.23	7.76	−3.4		

3.2. Seasonal, Daily, and Hourly Variations

The micrometeorological measurement was performed from summer to winter (19 July 2019 to 23 July 2020). The subsoil measurement system of CO_2 using FTIR started on 23 July 2019, sustaining approximately two days of continuous measurement on each visit due to power supply limitation. Meanwhile, the auxiliaries data both from the subsoil monitoring system and lattice tower which include soil temperature at various depth (Figure 5a), air pressure at different depth (Figure 5b), Soil Water Content (Figure 5c), precipitation (Figure 5c), CO_2 molar fraction at 1 and 6 m depth (Figure 5d), and friction velocity (Figure 5d) were measured continuously and simultaneously during monitoring periods.

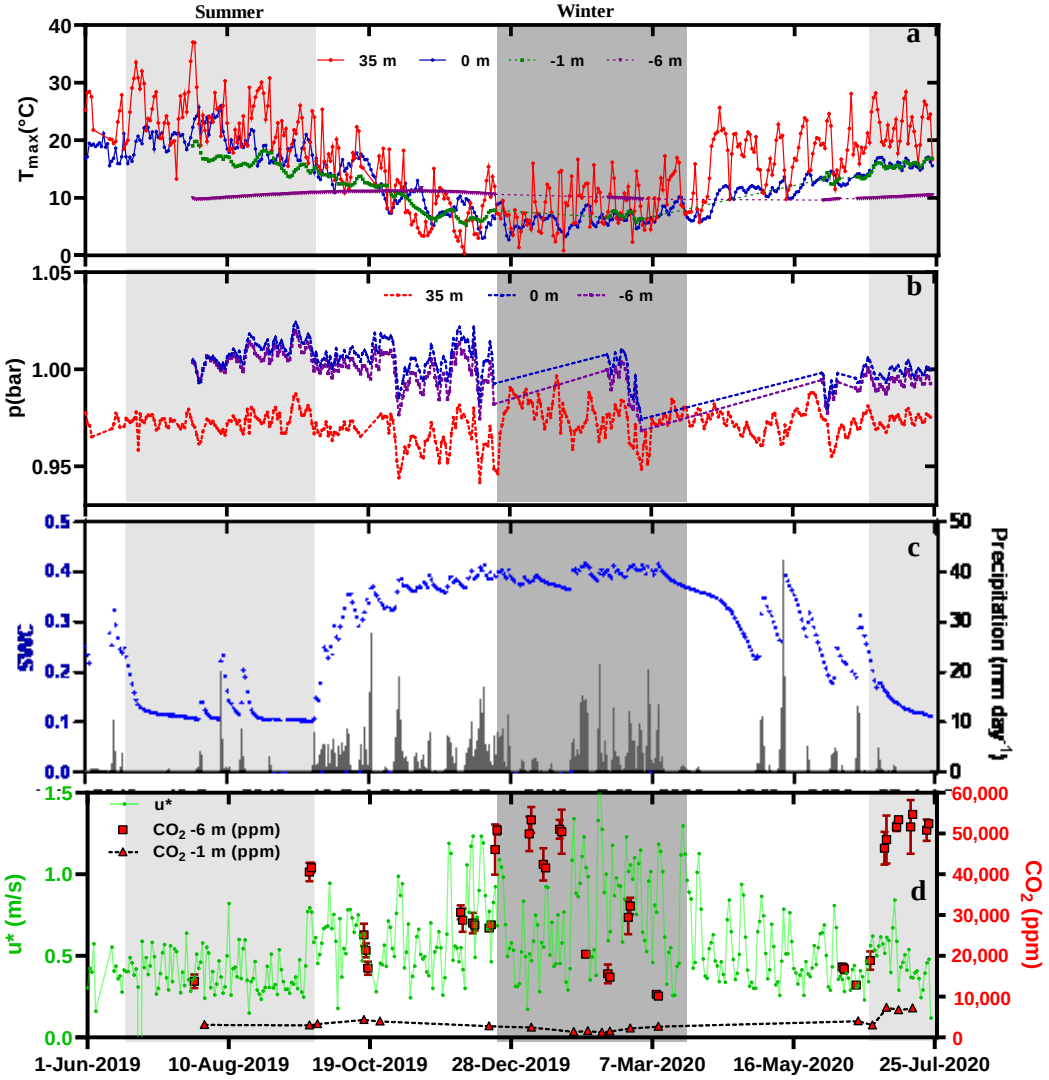

Figure 5. Time-series graph showing the daily max of temperature at various depth (35 m, 0 m, −1 m, and −6 m) (**a**), the daily average of atmospheric pressure measured at 35 and 0 m, and the soil-air pressure measured at 6m depth (**b**), soil water content (SWC) (**c**), precipitation (**c**), CO_2 molar fraction (χc) at 1 and 6 m depth (**d**), and friction velocity (**d**).

Overall, the atmospheric temperature ranged from −2 °C to 38 °C (Figure 5a). The atmospheric temperature at 35 m shows a clear seasonal pattern where it was highest in summer 2019 at 38 °C, and it started to decline significantly during the Autumn. The Temperature variations at −1 m and −6 m were found at 14.98–19.80 °C and 9.73–11.13 °C, respectively. The diurnal atmospheric temperature variations are also considered more significant than soil temperature (0 m), subsoil temperature at −1 m, and −6 m.

Even though there is a small difference in magnitude between the atmospheric pressure (35 m) and soil-air pressure (−6 m) around 150 mbar, the general pattern seasonally over the monitoring periods is similar. Although small differences in magnitude were identified, the daily average of atmospheric pressure (35 m and 0 m) and soil-air pressure (−6 m) shows a visually similar general pattern (Figure 5b). The atmospheric pressure at 35 m high indicates the lowest value, followed by soil air pressure at 6 m depth and soil interface (0 m) consecutively. The atmospheric pressure ranged from 0.933 to 0.998 at 35 m, 0.971 to 1.026 bar at 0 m, and 0.964 to 1.021 at −6 m. It is clear that the highest atmospheric pressure (35 m) was found in Summer and the lowest in winter. The daily average of soil water content (Figure 5c) demonstrates a clear correlation with precipitation and anticorrelation with temperature and very pronounced seasonal variation. The average lowest SWC occurred in summer at around 10%, with some spikes due to the rainfall episodes. However, this increase in SWC of approximately 20% lasted only around five days after the rainfall. During the winter, the average SWC remained high at around 40% due to more frequent rainfall and low temperatures. A slight reduction of SWC by approximately 5% was identified from January to February due to less frequent rain events.

Figure 5d, the daily χc (ppm) at −1 and −6 m and friction velocity (u*) above the canopy are provided. The daily average of friction velocity (u*) was relatively higher during the winter (0.7 m/s) than in summer (0.4 m/s). The χc generally increases as the depth, from the near-atmospheric layer (−1 m) up to a few meters to the subsoil layer (−6 m). This study demonstrates that subsoil CO_2 at 1 m depth is constantly lower than subsoil CO_2 at 6 m depth ranging from 1000–7000 ppm at −1 and 10,000–60,000 ppm at −6 m. The χc at −1 m was at the lowest in winter and highest in summer in June 2020. Meanwhile, the seasonal variation of χc at −6 m is somewhat weak. However, it can be seen that the rise of χc at −6 m depth occurs together with the fall of u* and the decrease in SWC due to the absence of rainfall. The seasonal variation of u* is also weak, where it is found to be low during summer and higher during winter, with an exception in early December 2019 to the end of February 2020. To better understand the general relationship between variables statistically, the matrix correlation based on Pearson's is provided in Figure 6.

The heatmap based on hourly data (Figure 6) between observed variables from 1 June 2019 to 23 July 2020 shows that the influence of temperature m on subsoil CO_2 concentration at −6 m was very pronounced with an R of 0.94 (T_{soil} at −1 m) and 0.83 (T_{soil} at 0 m). The CO_2 concentration at −6 m was also weakly inversely correlated with atmospheric pressure at 0 m (R: −0.59), soil-air pressure at −6 m (R: −0.48), SWC (R: −0.50), and soil temperature at −6 m (R: −0.59). However, a strong correlation between temperature and soil CO_2 does not extend to the shallower depth of −1 m. Pearson's CO_2 concentration at −1 m with soil temperature at −1 m and 0 m were −0.36 to 0.14 consecutively. This relatively low correlation is most likely due to time window measurement inconsistency. While all temperature data were measured hourly during the monitoring campaign, χc at −1 m was measured only once every visit during midday. Furthermore, the heat map demonstrates a pronounced pattern between soil temperature at various depths and SWC with R more significant than −0.7, except for soil temperature at −6 m. To better understand the driving mechanism of CO_2 concentration at −6 m during dry and wet periods and weather correlation between subsoil CO_2 concentrations extends to seasonal timescales, Principle Component Analysis (PCA) and time series of hourly data corresponding to observed variables are provided in Figure 7.

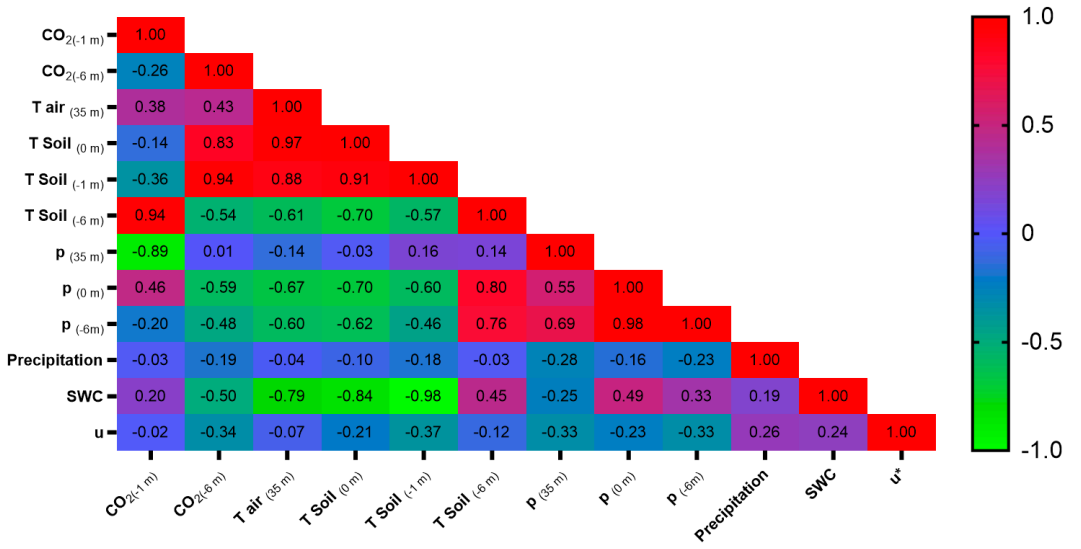

Figure 6. Heat map based on Pearson's correlation test matrix of and hourly data including CO_2 molar fraction (-1 m and -6 m) (χc), soil water content (SWC), u* (friction velocity), temperature$_{(max)}$ (T, at -6 m and 0 m), soil air pressure (-6 m), atmospheric pressure (p, at 35 m and 0 m), and precipitation (P). The correlations were calculated when there was a measurement of CO_2 at -6 m.

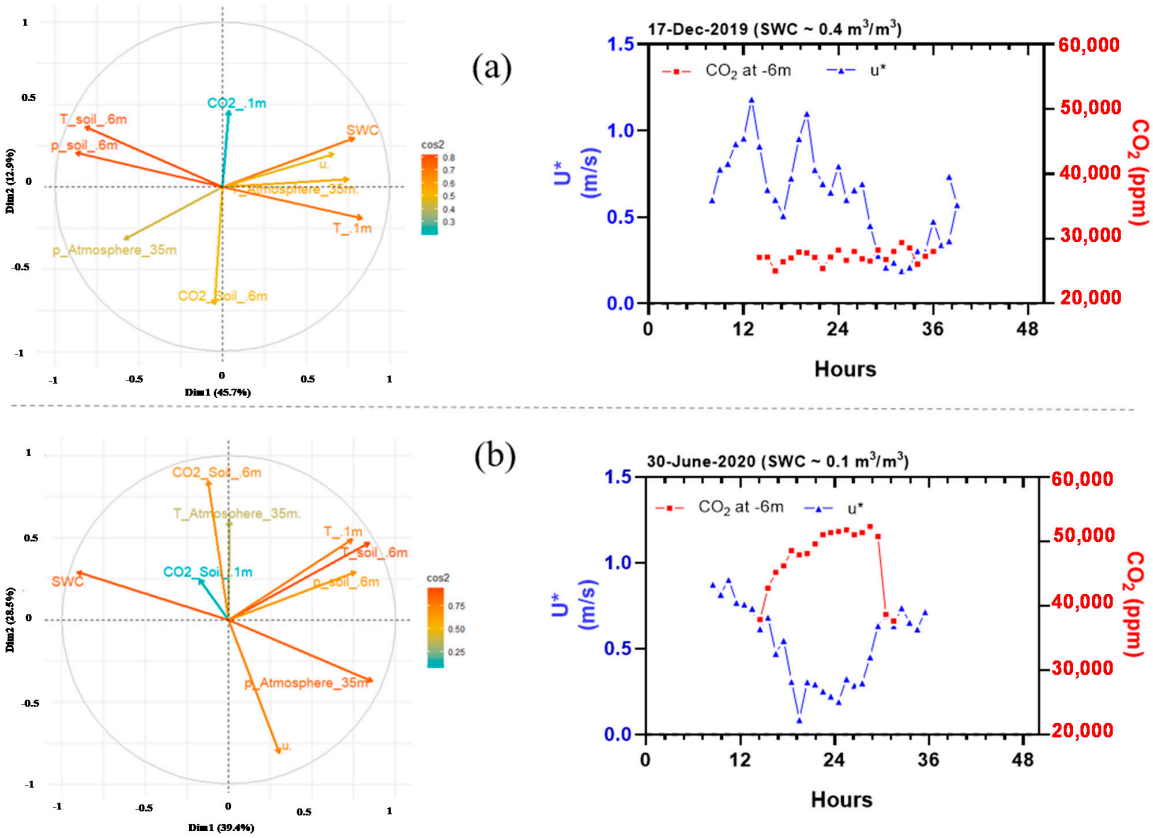

Figure 7. The left side of the figure indicates the principal component analysis (PCA) of hourly data spanning from 19 September 2019 to 23 July 2020, and the right side shows an intraday variation of hourly u* and CO_2 during 48 h. Part a corresponds to wet periods (SWC > 0.2 m^3/m^3), and Part b represents dry periods (SWC $\leq$ 0.2 m^3/m^3).

Figure 7 focuses on a principal component analysis (PCA) and hourly variations of χc at 6 m depth auxiliaries data. The color affected the different parameters refers to the significance of the variables (cos^2) expressed between 0 (bad defined) and 1 (well defined). It can be seen from PCA that CO_2 at 6 m depth during low SWC (Figure 7b) is inversely correlated with u* with cos^2 above 0.75. A graph showing intraday variation firmly confirms the inverse relationship with identical rises and falls on the right side. The χc at 6 m depth decreased by more than 10,000 ppm, following an increase of u*, from 0.2 m/s to 0.8 m/s. However, this pattern does not apply in observation during the wet period (Figure 7a), where PCA fails to define the relationship between CO_2 at −6 m with other variables. The intraday graph on the right side does not indicate a pronounced negative correlation pattern.

4. Discussion

4.1. Field Performances and Processing Infrastructure

Even though this work aims to develop a continuous flow system to continuously measure the soil gas concentration and the variability of physical parameters, it can also be used as preliminary guidelines to better understand the CO_2 variations in the forest ecosystem. Figure 8 shows a typical infrared profile of gas coming from the borehole at 6 m depth, where only the absorption bands of CO_2 and H_2O are clearly visible. Even though CH_4 concentration was always below our IR sensor's sensibility limit, it was still detectable with an ex-situ GC analysis at a range of 0.9–2.7 ppm with minor depth-dependence. Moreover, these monitoring stations have shown that soil CO_2 concentration monitoring can be maintained long term without grid power. After deployment, there were follow-up visits to change the batteries every month before December 2019 and every week after December 2019, but cumulatively these equated to only a few fieldwork days. During the deployments, the average power consumption for two days of continuous and simultaneous measurements was roughly 300 A. This includes the power demand from a laptop, FTIR, auxiliary sensors, and circulation module (pumps). Nonetheless, the advantages outweighed the drawback of its power consumption, where the other actively IR gas interfinger can be identified individually.

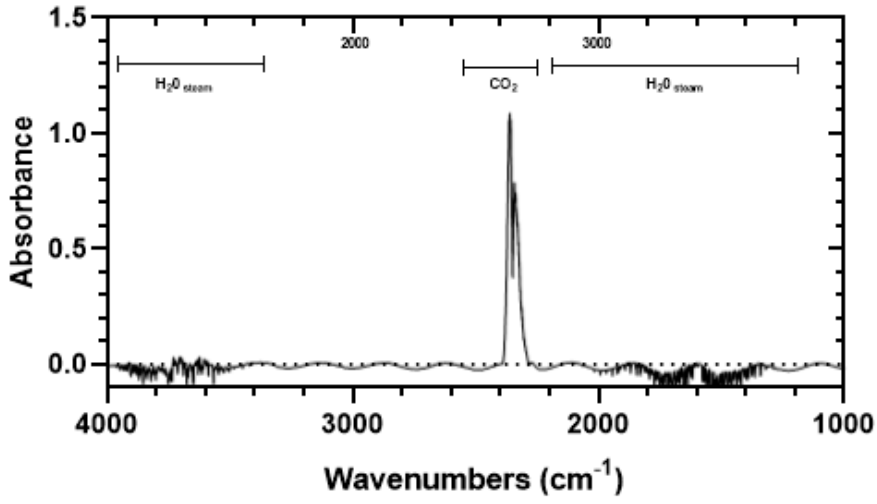

Figure 8. Typical infrared profile of soil gas from the 6 m borehole (Time: 20:03 on 16/Oct/2019). Interferences weak bands of H_2O_{vapour} are also visible on the spectrum at the low and high-frequency range.

The FTIR calibration was deemed very simple considering CO_2 vibrational mode at the wavelength of 2400 cm^{-1} (v_3). The high-frequency data hold many exciting features that are not captured in the synoptic data sets and will be useful for tuning our understanding

of soil carbon. With this study, this monitoring infrastructure was considerably successful in terms of survivability and management. In the case of continuously accessible power, the system could record and store high-frequency measurements (<1 min). There is also an opportunity to reduce power consumption by eliminating an FTIR Bruker alpha and a laptop while relying only on low power consumption, an IR sensor, and a data logger. Since the FTIR measurement with a resolution of 1 cm^{-1} and 4 cm^{-1} is visually identical with a polynomial model, the linear model fitting was applied for both resolutions provided in Table 2. Therefore, it is important to understand how FTIR's lower resolution at 4 cm^{-1} performs in conjunction with the Beer-Lambert law.

Table 2. The linear fitting comparison between FTIR resolution of 1 cm^{-1} and 4 cm^{-1}.

FTIR Resolution	Equation	Adjusted R^2
1 cm^{-1}	Y = 640 × −781	0.987
4 cm^{-1}	Y = 650 × −1351	0.976

The resolution of 1 cm^{-1} has a slightly higher correlation index using a linear model than 4 cm^{-1} at 0.987 and 0.976, respectively. It has been reported that the equation between the partial pressure of CO_2 and CH_4 does not follow the beer-lambert law, especially if it is measured using the spectral resolution of fewer than 1 cm^{-1} [43,47]. Unlike solid or liquid, which does not possess a rotational mode, the gas state involves vibrational and rotational transitions. In the case of gases calibration, the rotation of the bands is often thin (FWHM [Full width at half maximum] < 0.2 cm^{-1}), and all the spectral lines that make them are only detectable if a very high resolution (of the order of 0.1 cm^{-1}) is used. The area derived from lower resolution FTIR does not precisely match the sum of all the theoretical spectral lines of vibration-rotation. Hence, it is almost certain the calibration curves fit with a three-degree polynomial equation rather than a linear equation result from its low-resolution measurement. However, considering the longer scanning time resulting in lower temporal resolution, the 3-degree polynomial is deemed acceptable for producing a calibration curve.

4.2. CO_2 Molar Fraction Dynamics

It is almost certain that CO_2 concentrations vary depending on physicochemical properties, soil cover types, and climatic conditions. However, the CO_2 change between forest land and grassland is similar to approximately 100 to 1300 mg CO_2 m^2 h^{-1} than barren land and cropland [3]. The ranges of CO_2 concentration measured at the grassland in Kyushu Island, Japan was around 1300–8700 ppm (0.1 m depth), 2500–10,800 ppm (0.2 m depth), 4200–13,200 ppm (0.3 m depth), and 5800–16,500 ppm (1.0 m depth) [48]. It has also been reported that the soil CO_2 concentration measured at a depth of 0.3 m in the South-Moravian region was around 5000 to 8000 ppm [49]. The soil CO_2 concentrations in our forest site are more comparable with a study conducted previously in a temperate deciduous forest using NDIR that ranged between 774 ppm and 6521 ppm at 1 m depth [50]. Higher CO_2 concentration at a depth less than 1 m has also been reported in forest site Meurthe et Moselle, France, with around 20,000 ppm at 60 cm depth [51] and a study conducted in a temperate forest located at Shale Hills Critical Zone Observatory, Pennsylvania, US, reported that the CO_2 concentration reached up to 50,000 ppm at a depth of 1.5 m, attributed to the greater root respiration depth partly due to higher macroporosity of sandstone lithologies [52]. The CO_2 concentration above 10% is generally found in the active geothermal area with a significant pressure gradient transport instead of the solely diffusive process [24,25]. Some studies suggest a strong positive correlation between χc and temperature [3,49,53], where temporal CO_2 concentration is affected by soil temperature on a biweekly basis [50]. Our work demonstrates that CO_2 and temperature are positively correlated at 1 and 6 m depth. In a temperate forest, the temperature is considered the primary driver of heterotrophic soil respiration, releasing CO_2 as organisms decompose

soil organic carbon (SOC) [54–56]. However, the effects of soil temperature toward heterotrophic respiration are rather complex [57]. It might also indirectly affect the microbial, substrate quantity, and substrate availability on a daily to annual basis [53,54]. On minutes to an hourly basis, it might also influence the enzyme activity produced by bacteria and fungi [58].

Furthermore, most of the studies carried on in the forest soil mainly focused at a depth of 0 to 1 m, where the soil CO_2 production is often a correlation to biological activity is more instantaneous. Very little data are available on the evolution of the CO_2 concentration in the deepest layers of the soil. In the present study, the abiotic drivers' relationship, including SWC and u*, is further explored and provided in Figure 9.

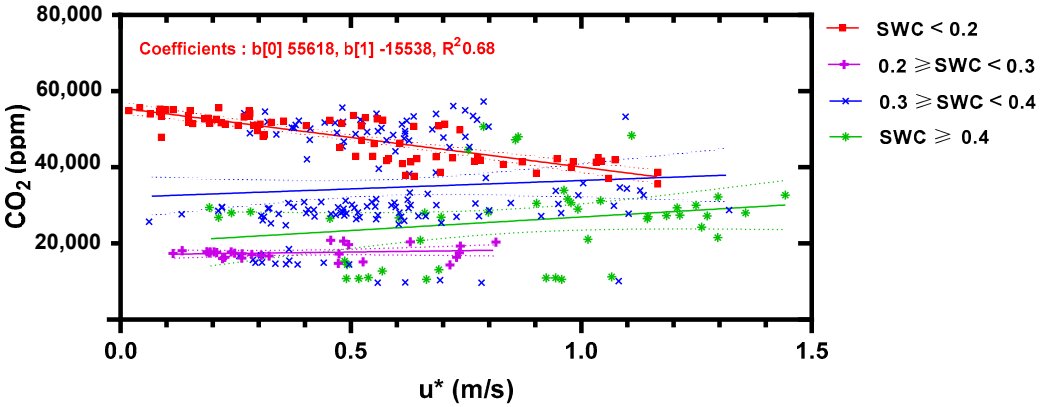

Figure 9. The relationship between hourly CO_2 molar fraction (χc) at 6m depth and friction velocity (u*) above the canopy for different levels of SWC.

4.3. Analysis of Wind Turbulence and Soil Water Content

Several periods with high and low friction velocity were detected during the monitoring period (Figure 9) where the relationship between friction velocity and soil CO_2 concentration at −6 m is very pronounced, especially during dry periods with R^2 of 0.6 where SWC is less than 0.2 m^3/m^{-3} ($CO_2 = -14{,}882u^* + 55{,}066$). However, this relationship does not extend during wet periods where SWC is above 0.2 m^3/m^3.

This finding acts as empirical evidence of subsoil ventilation and the importance of advection in gas transport processes where the decrease of χc coincides with high u* that fits with the linear model (coefficients: b[0] 55,066, b[1] −14,882, R^2: 0.68) (Figure 9). Some previous works focusing on soil CO_2 dynamics have reported the influence between χc and u* [26,31,59]. The lower soil of our site consists of sandy and clayey passages caused by the complex sedimentary source material. The calcareous bedrock mainly consisted of calcium carbonate and a few amounts of clay minerals surrounded by the weathered layer rich in clays due to decarbonization. It is a widely held view that limestone's solubility in weak acid and limestone, resulting in karst forming processes. It has been previously studied that the karst system stores a large amount of CO_2 underground, which later was emitted during windy days and filled quickly during low wind speed through cracks and fissures [59]. Even though some sinkholes in our site are visible, this hypothesis needs further investigation to understand the rate and magnitude of calcite dissolution. Also, monitoring data suggest that the subsoil's permeability is most likely reduced during wet periods diminishing molecular diffusion and advection. The lower the SWC value, the more enormous the ventilation's potential to remove CO_2 from the soil, as indicated by previous works in a karstic environment [59,60].

It is widely known that the increase of temperature by 10 °C leads to a higher respiration rate factor, known as temperature sensitivity of soil respiration, that is often expressed as the Q10 [61,62]. However, this factor related to biological activity cannot fully explain the variation. Instead, the CO_2 fluctuation is likely due to pressure pumping effects (PPE)

promoted by u* fluctuation where the soil acts as a semi-permeable membrane storing and releasing CO_2 [33,63,64]. The continuous wavelet-based analysis (Figure 10) was employed of the dataset from 17 June to 23 July 2020, which was chosen due to the dataset's continuity. The wavelet analysis was done using R software and Waveletcomp Package [44,65] to test our hypothesis regarding pressure pumping effects generated in a deep soil layer.

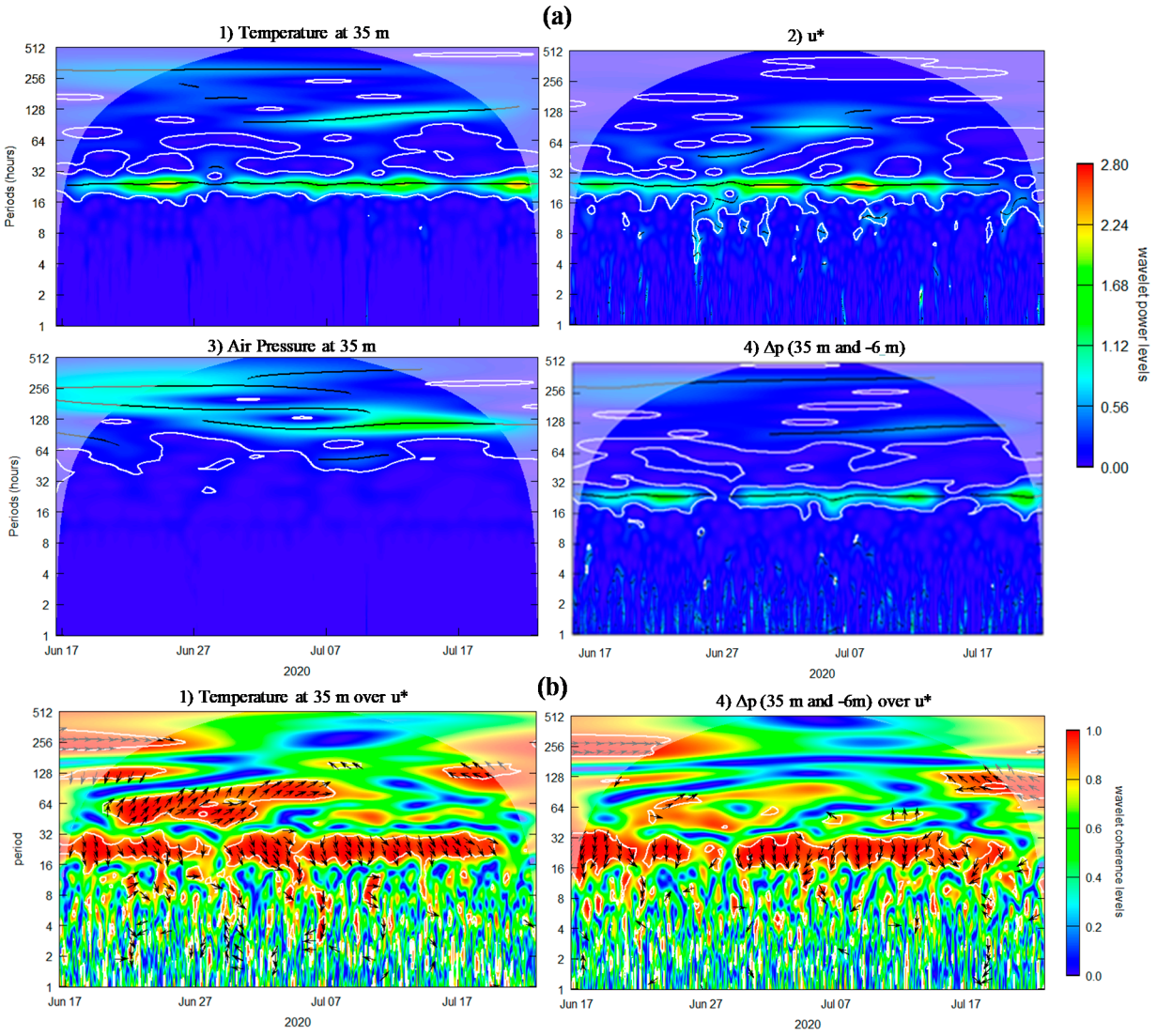

Figure 10. Half-hourly wavelet-based analysis from 17 June to 23 July 2020 which include (**a**) wavelet power spectrum of (**a1**) temperature at 35 m, (**a2**) friction velocity (u*), (**a3**) air pressure at 35 m, and (**a4**) air pressure difference (Δp) between 35 m and −6 m. Moreover, wavelet coherence analysis (**b**) shows the multivariate statistical significance of (**b1**) temperature at 35 m over u* and (**b2**) Δp over u*. In part, a reddish area and black lines represent high wavelet power levels. In part b, the red area with white contour lines demonstrates a high correlation with more than 5% significance levels. Arrows represent a multivariate phase-locked angle relationship where horizontal arrows pointing left (phase angle: 180°) indicates that two wavelet series are out of phase and horizontal arrows pointing right (phase angle: 0°) suggests that two wavelet series are in phase. A white shaded area indicates that the time series are influenced by edge effects.

Friction velocity (u*) and temperature (35 m) recorded from the 17 June to 23 July 2020 ranged from 0 m/s–1 m/s and 10–28 °C, respectively. Wavelet power analysis of temperature and u* (Figure 10a(1,2)) demonstrates substantial diurnal scale as expected shown by maximum power wavelet at periods of 24 (24 h). Wavelet power levels of u* in periods of 24 were slightly higher with 3.33 compared to temperature with 2.87, indicating more pronounce daily variation. As for the air pressure, even though the pressure above

the canopy (35 m), soil-air interface pressure (0 m), soil-air pressure (−6 m) shows different values of magnitude, the general patterns are similar; therefore, a wavelet power analysis was employed only to the air pressure at 35 m. In contrast with the temperature (35 m) and u*, the air pressure at 35 m shows little or no daily variations. Instead, the wavelet power levels of air pressure at 35 m (Figure 10a(3)) were significant at the region of 128 (5 days) with only 1.74, which was also found in a wavelet power analysis of temperature (35 m). What is striking in the wavelet power analysis is that the pressure difference (Δp, 35 m and −6 m) provided in Figure 10a(4) shows strong daily fluctuation shown by dominant periods of 24 similar to temperature (35 m) and u*. However, these data should be interpreted carefully since the pressure sensor's resolution was only 0.002 bar and could not detect smaller pressure fluctuation. The pressure fluctuation in the frequency ranging from 0.01 Hz–0.1 Hz is highly dependent on the above canopy wind speed [66]. The pressure dynamics that might be generated from pressure pumping effects due to wind turbulence above the canopy must be further investigated. According to wavelet coherence analysis, the temporal correlation between the temperature at 35 m over u* (Figure 10b(1)) and Δp (35 m and −6 m) over u* (Figure 10b(2)) demonstrated substantial variation, especially at a daily scale with time lags of temperature (35 m) and Δp (35 m and −6 m) over u* ranged from 2 to 4 h. Besides the temperature, Δp between soil air interface and soil-air is highly likely to promote the contraction and expansion of the air stored in soil pores, cracks, and fissures, which play a significant role in regulating the vertical transport and gas storage suggested by previous works [33,67,68]. Nonetheless, propagation of atmospheric pressure fluctuations into the subsurface has been known to promote the air's migration in moderately permeable materials up to 10 m depth and even greater depth in a fractured rock system [69–71]. However, most works on assessing the PPE and wind turbulence CO_2 focus on the top layer up to one-meter depth; our work provides empirical evidence of a strong partial relationship on a deeper soil layer (6 m).

5. Conclusions

We describe the calibration technique, observational setup of the measurement campaign, aspects of the data analysis, and instrument field analysis of the recorded time series of soil gases and auxiliaries data within the study area. This soil gas measurement infrastructure combining borehole measurement with micrometeorological measurement offers excellent possibilities for long-term in-situ and continuous gas monitoring to derive the vertical distribution of CO_2. Thus, this infrastructure allowed the observation of the temporal dynamics in soil-gas CO_2 research. Relatively short-term events could be monitored, notably those associated with pressure and temperature at a deep soil layer, which is difficult to measure using a conventional method. Besides, the long-term data set of soil gas baseline will contribute to understanding better the influence of short-term events, including (i) spikes of short-term event, (ii) magnitudes of change caused by the suspected driving variables, (iii) the duration of the changing circumstances, and (iv) indirect variables influencing these short-term events. Such a metrology approach will contribute to the definition of good practice for the state of studies related to subsoil CO_2 molar fraction in conjunction with the soil-air pressure and temperature. Even though this approach has been applied to the forest ecosystem, it can be extended to any other natural or anthropic systems. Even though CH_4 concentration was always below our IR sensor's sensibility limit, this infrastructure might still be applied in CH_4-rich site.

Furthermore, this study shows substantial empirical pieces of evidence that the increase of temperature leads to higher respiration rates, which further produced CO_2 stored in deep soil layers. However, this factor related to biological activity cannot fully explain the variation. We hypothesize pressure pumping effects also play a role, especially during dry summer. The decreases of CO_2 molar fraction in the subsoil coincided with high turbulence, resulting in increased CO_2 storage in deep soil during low turbulence. This study also demonstrates that permeability significantly reduced during wet periods diminishing the molecular diffusion and advection. All of these highlight the importance of

spatial and temporal dynamics of deep soil CO_2 dynamics that reach a value of up to 100 times larger than atmospheric CO_2. This empirical evidence also challenges the current assumption that the influence of PPE is only significant on a topsoil layer. However, it is still uncertain whether this strong relationship is site-specific or not since it is highly likely that the soil porosity, soil texture, stand type, and canopy height play roles. As flux tower establishment expands, there is a strong need to apply borehole measurement underneath to understand better the relationships between friction velocity and subsoil CO_2 dynamics on various sites.

Author Contributions: Conceptualization, D.A., P.D.D., L.S.-A., and O.B.; methodology, O.B., C.G., G.N., M.P., and M.D.; software, D.A.; validation, O.B., G.N.; formal analysis, D.A.; investigation, D.A., P.D.D., and O.B.; resources, C.G., M.P., and M.D.; data curation, D.A.; writing—original draft preparation, D.A.; writing—review and editing, P.D.D., L.S.-A., and O.B.; visualization, D.A.; supervision, P.D.D., L.S.-A.; project administration, P.D.D., L.S.-A.; funding acquisition, P.D.D., L.S.-A. All authors have read and agreed to the published version of the manuscript.

Funding: This work was supported partly by the French PIA project "*Lorraine Université d'Excellence*", reference ANR-15-IDEX-04-LUE.

Informed Consent Statement: Not applicable.

Data Availability Statement: The data presented in this study are available on request from GeoRessources Laboratory.

Acknowledgments: We wish to thank Aurélien Randi for his excellent technical assistance on the calibration experiment. Special thanks go to Maxime Simon for his technical assistance in managing the flux tower data. We also thank Van Hoan Le and Catherine Lorgeoux for their meticulous work on gas chromatography calibration. The authors wish to thank the reviewers for their valuable comments. We also thank the French National Forest Office (ONF) for supporting the installation of the monitoring site. The forest observatory of *Montiers-sur-Saulx* belongs to Andra's long term observatory (Ope) and is jointly managed by Andra and INRAE. This forest observatory is integrated in the research infrastructures ANAEE France and ICOS Fr. The UR BEF, one of the research units contributing to the present study, is supported by the French National Research Agency through the Laboratory of Excellence ARBRE (ANR-11-LABX-0002-01).

Conflicts of Interest: The authors declare no conflict of interest.

References

1. Angert, A.; Yakir, D.; Rodeghiero, M.; Preisler, Y.; Davidson, E.A.; Weiner, T. Using O_2 to study the relationships between soil CO_2 efflux and soil respiration. *Biogeosciences* **2015**, *12*, 2089–2099. [CrossRef]
2. Friedlingstein, P.; Jones, M.W.; O'Sullivan, M.; Andrew, R.M.; Hauck, J.; Peters, G.P.; Peters, W.; Pongratz, J.; Sitch, S.; Le Quéré, C.; et al. Global carbon budget 2019. *Earth Syst. Sci. Data* **2019**, *11*, 1783–1838. [CrossRef]
3. Oertel, C.; Matschullat, J.; Zurba, K.; Zimmermann, F.; Erasmi, S. Greenhouse gas emissions from soils—A review. *Chemie der Erde - Geochemistry* **2016**, *76*, 327–352. [CrossRef]
4. Schacht, U.; Jenkins, C. Soil gas monitoring of the Otway Project demonstration site in SE Victoria, Australia. *Int. J. Greenh. Gas Control* **2014**, *24*, 14–29. [CrossRef]
5. Taquet, N.; Pironon, J.; De Donato, P.; Lucas, H.; Barres, O. Efficiency of combined FTIR and Raman spectrometry for online quantification of soil gases: Application to the monitoring of carbon dioxide storage sites. *Int. J. Greenh. Gas Control* **2013**, *12*, 359–371. [CrossRef]
6. Schlömer, S.; Möller, I.; Furche, M. Baseline soil gas measurements as part of a monitoring concept above a projected CO_2 injection formation-A case study from Northern Germany. *Int. J. Greenh. Gas Control* **2014**, *20*, 57–72. [CrossRef]
7. Kim, J.; Yu, S.; Yun, S.T.; Kim, K.H.; Kim, J.H.; Shinn, Y.J.; Chae, G. CO_2 leakage detection in the near-surface above natural CO_2-rich water aquifer using soil gas monitoring. *Int. J. Greenh. Gas Control* **2019**, *88*. [CrossRef]
8. Kim, Y.S. Soil-Atmosphere Exchange of CO_2, CH_4 and N_2O in Northern Temperate Forests: Effects of Elevated CO_2 Concentration, N Deposition and Forest Fire. *Eurasian J. For. Res.* **2013**, *16*, 1–43. [CrossRef]
9. Barba, J.; Cueva, A.; Bahn, M.; Barron-Gafford, G.A.; Bond-Lamberty, B.; Hanson, P.J.; Jaimes, A.; Kulmala, L.; Pumpanen, J.; Scott, R.L.; et al. Comparing ecosystem and soil respiration: Review and key challenges of tower-based and soil measurements. *Agric. For. Meteorol.* **2018**, *249*, 434–443. [CrossRef]

10. Hoffmann, M.; Jurisch, N.; Albiac, E.; Hagemann, U.; Drösler, M.; Sommer, M.; Augustin, J. Automated modeling of ecosystem CO_2 fluxes based on periodic closed chamber measurements: A standardized conceptual and practical approach. *Agric. For. Meteorol.* **2015**, *200*, 30–45. [CrossRef]
11. Pokryszka, Z.; Adelise, F.; FARRET, R.; Lafortune, S.; MICHEL, E.; Rupasinghe, S. *Values of Reference of the Flux of CO_2 and CH_4 from Natural Soil Biogenic Origin*; Ineris: Paris, France, 2017.
12. Sánchez-Cañete, E.P.; Barron-Gafford, G.A.; Chorover, J. A considerable fraction of soil-respired CO_2 is not emitted directly to the atmosphere. *Sci. Rep.* **2018**, *8*, 2–11. [CrossRef]
13. Klosterhalfen, A.; Moene, A.F.; Schmidt, M.; Scanlon, T.M.; Vereecken, H.; Graf, A. Sensitivity analysis of a source partitioning method for H_2O and CO_2 fluxes based on high frequency eddy covariance data: Findings from field data and large eddy simulations. *Agric. For. Meteorol.* **2019**, *265*, 152–170. [CrossRef]
14. Eder, F.; De Roo, F.; Rotenberg, E.; Yakir, D.; Schmid, H.P.; Mauder, M. Secondary circulations at a solitary forest surrounded by semi-arid shrubland and their impact on eddy-covariance measurements. *Agric. For. Meteorol.* **2015**, *211–212*, 115–127. [CrossRef]
15. Aubinet, M.; Vesala, T.; Papale, D. (Eds.) *Eddy Covariance: A Practical Guide to Measurement and Data Analysis*; Springer Science & Business Media: Dordrecht, The Netherlands, 2012; ISBN 9788578110796.
16. Wang, Y.; Li, X.; Dong, W.; Wu, D.; Hu, C.; Zhang, Y. Depth-dependent greenhouse gas production and consumption in an upland cropping system in northern China. *Geoderma* **2018**, *319*, 100–112. [CrossRef]
17. Phillips, C.L.; Bond-Lamberty, B.; Desai, A.R.; Lavoie, M.; Risk, D.; Tang, J.; Todd-Brown, K.; Vargas, R. The value of soil respiration measurements for interpreting and modeling terrestrial carbon cycling. *Plant Soil* **2016**, 1–25.
18. Maier, M.; Schack-Kirchner, H. Using the gradient method to determine soil gas flux: A review. *Agric. For. Meteorol.* **2014**, *192–193*, 78–95. [CrossRef]
19. Sánchez-ca, E.P.; Kowalski, A.S. Comment on "Using the gradient method to determine soil gas flux: A review" by M. Maier and H. Schack-Kirchner. *Agric. For. Meteorol.* **2014**, *197*, 254–255. [CrossRef]
20. Smith, K.A.; Ball, T.; Conen, F.; Dobbie, K.E.; Massheder, J.; Rey, A. Exchange of greenhouse gases between soil and atmosphere: Interactions of soil physical factors and biological processes. *Eur. J. Soil Sci.* **2003**, *54*, 779–791. [CrossRef]
21. Kowalski, A.S.; Serrano-Ortiz, P.; Janssens, I.A.; Sánchez-Moral, S.; Cuezva, S.; Domingo, F.; Were, A.; Alados-Arboledas, L. Can flux tower research neglect geochemical CO_2 exchange? *Agric. For. Meteorol.* **2008**, *148*, 1045–1054. [CrossRef]
22. Wang, K.; Liu, C.; Zheng, X.; Pihlatie, M.; Li, B.; Haapanala, S.; Vesala, T.; Liu, H.; Wang, Y.; Liu, G.; et al. Comparison between eddy covariance and automatic chamber techniques for measuring net ecosystem exchange of carbon dioxide in cotton and wheat fields. *Biogeosciences* **2013**, *10*, 6865–6877. [CrossRef]
23. Rose, A.W.; Hawkes, H.E.; Webb, J.S. *Geochemistry in Mineral Exploration*, 2nd ed.; Academic Press: London, UK, 1979; Volume 95.
24. Pearce, J.; Czernichowski-Lauriol, I.; Lombardi, S.; Brune, S.; Nador, A.; Baker, J.; Pauwels, H.; Hatziyannis, G.; Beaubien, S.; Faber, E. A review of natural CO_2 accumulations in Europe as analogues for geological sequestration. *Geol. Soc. Spec. Publ.* **2004**, *233*, 29–41. [CrossRef]
25. Camarda, M.; De Gregorio, S.; Favara, R.; Gurrieri, S. Evaluation of carbon isotope fractionation of soil CO_2 under an advective—Diffusive regimen: A tool for computing the isotopic composition of unfractionated deep source. *Geochim. Cosmochim. Acta* **2007**, *71*, 3016–3027. [CrossRef]
26. Maier, M.; Aubinet, M. Turbulence Effect on Gas Transport in Three Contrasting Forest Soils. *Soil Sci. Soc. Am. J.* **2011**. [CrossRef]
27. Holton, J.R.; Hakim, G.J. *An Introduction to Dynamic Meteorology: Fifth Edition*; Elsevier Academic Press: Boston, MA, USA, 2012; Volume 9780123848, ISBN 9780123848666.
28. Streeter, V.L.; Wylie, E.B. *Fluid Mechanics*, 6th ed.; McGraw-Hill: Singapore, 1983.
29. Inoue, T.; Glud, R.N.; Stahl, H.; Hume, A. Comparison of three different methods for assessing in situ friction velocity: A case study from Loch Etive, Scotland. *Limnol. Oceanogr. Methods* **2011**, *9*, 275–287. [CrossRef]
30. Nawaz, M.F.; Bourrié, G. Soil compaction impact and modelling. A review. *Agron. Sustain. Dev.* **2013**, 291–309. [CrossRef]
31. Sánchez-cañete, E.P.; Oyonarte, C.; Serrano-ortiz, P.; Yuste, J.C.; Pérez-priego, O.; Domingo, F.; Kowalski, A.S. Winds induce CO_2 exchange with the atmosphere and vadose zone transport in a karstic ecosystem. *J. Geophys. Res. Biogeosci.* **2016**, 2049–2063. [CrossRef]
32. Maier, M.; Longdoz, B.; Laemmel, T.; Schack-kirchner, H.; Lang, F. 2D profiles of CO_2, CH_4, N_2O and gas diffusivity in a well aerated soil: Measurement and Finite Element Modeling. *Agric. For. Meteorol.* **2017**, *247*, 21–33. [CrossRef]
33. Laemmel, T.; Mohr, M.; Longdoz, B.; Schack-kirchner, H.; Lang, F.; Schindler, D.; Maier, M. From above the forest into the soil—How wind affects soil gas transport through air pressure fluctuations. *Agric. For. Meteorol.* **2019**, *265*, 424–434. [CrossRef]
34. Schloemer, S.; Furche, M.; Dumke, I.; Poggenburg, J.; Bahr, A.; Seeger, C.; Vidal, A.; Faber, E. A review of continuous soil gas monitoring related to CCS—Technical advances and lessons learned. *Appl. Geochem.* **2013**, *30*, 148–160. [CrossRef]
35. Adisaputro, D.; Saputra, B. Carbon Capture and Storage and Carbon Capture and Utilization: What Do They Offer to Indonesia? *Front. Energy Res.* **2017**, *5*, 2012–2015. [CrossRef]
36. Lafortune, S.; Gombert, P.; Pokryszka, Z.; Lacroix, E.; de Donato, P.; Jozja, N. Monitoring scheme for the detection of hydrogen leakage from a deep underground storage. Part 1: On-site validation of an experimental protocol via the combined injection of helium and tracers into an aquifer. *Appl. Sci.* **2020**, *10*, 6058. [CrossRef]
37. Monne, J.; Jammes, L.; Gaucher, E.; Labat, N.; Urbancyk, C.; Thibeau, S.; Prinet, C.; Payre, X.; Schuhler, T.; Pourtoy, D.; et al. *Carbon Capture and Storage—The Lacq Pilot Project and Injection Periode 2006–2013*; Total: Paris, France, 2015; p. 276.

38. Tate, K.R. Soil methane oxidation and land-use change—From process to mitigation. *Soil Biol. Biochem.* **2015**, *80*, 260–272. [CrossRef]
39. Frey, M.; Hase, F.; Blumenstock, T.; Groß, J.; Kiel, M.; Mengistu Tsidu, G.; Schäfer, K.; Sha, M.K.; Orphal, J. Calibration and instrumental line shape characterization of a set of portable FTIR spectrometers for detecting greenhouse gas emissions. *Atmos. Meas. Tech.* **2015**, *8*, 3047–3057. [CrossRef]
40. Doyle, W.M. *Principles and applications of Fourier transform infrared (FTIR) process analysis*; Hellma-Axiom: CA, USA, 1992; Volume 2.
41. Naseska, M. Fourier Transform Infrared Spectroscopy. *Univ. Ljubljana* **2016**, 1–12. [CrossRef]
42. Smith, B.C. *Fundamentals of Fourier Transform Infrared Spectroscopy*; CRC Press: Boca Raton, FL, USA, 2011; ISBN 9781420069303.
43. Cailteau, C.; de Donato, P.; Pironon, J.; Vinsot, A.; Garnier, C.; Barres, O. In situ gas monitoring in clay rocks: Mathematical developments for CO_2 and CH_4 partial pressure determination under non-controlled pressure conditions using FT-IR spectrometry. *Anal. Methods* **2011**, *3*, 888. [CrossRef]
44. R Core Team. *R: A Language and Environment for Statistical Computing*; R Foundation for Statistical Computing: Vienna, Austria, 2020.
45. Kirchen, G.; Calvaruso, C.; Granier, A.; Redon, P.O.; Van der Heijden, G.; Bréda, N.; Turpault, M.P. Local soil type variability controls the water budget and stand productivity in a beech forest. *For. Ecol. Manag.* **2017**, *390*, 89–103. [CrossRef]
46. Calvaruso, C.; Kirchen, G.; Saint-André, L.; Redon, P.O.; Turpault, M.P. Relationship between soil nutritive resources and the growth and mineral nutrition of a beech (Fagus sylvatica) stand along a soil sequence. *Catena* **2017**, *155*, 156–169. [CrossRef]
47. Bak, J.; Larsen, A. Quantitative Gas Analysis with FT-IR: A Method for CO_2 Calibration Using Partial Least-Squares with Linearized Data. *Appl. Spectrosc.* **1995**, *49*, 437–443. [CrossRef]
48. Salmawati, S.; Sasaki, K.; Yuichi, S. Estimating Surface CO_2 Flux Based on Soil Concentration Profile. *Br. J. Environ. Clim. Chang.* **2017**, *7*, 214–222. [CrossRef]
49. Faimon, J.; Lang, M. What actually controls the minute to hour changes in soil carbon dioxide concentrations? *Geoderma* **2018**, *323*, 52–64. [CrossRef]
50. Jochheim, H.; Wirth, S.; von Unold, G. A multi-layer, closed-loop system for continuous measurement of soil CO_2 concentration. *J. Plant Nutr. Soil Sci.* **2018**, *181*, 61–68. [CrossRef]
51. Goutal, N.; Renault, P.; Ranger, J. Forwarder traffic impacted over at least four years soil air composition of two forest soils in northeast France. *Geoderma* **2013**, *193–194*, 29–40. [CrossRef]
52. Hodges, C.; Kim, H.; Brantley, S.L.; Kaye, J. Soil CO_2 and O_2 Concentrations Illuminate the Relative Importance of Weathering and Respiration to Seasonal Soil Gas Fluctuations. *Soil Sci. Soc. Am. J.* **2019**, *83*, 1167–1180. [CrossRef]
53. Delogu, E.; Longdoz, B.; Plain, C.; Epron, D. Seasonal and vertical variations in soil CO_2 production in a beech forest: An isotopic flux-gradient approach. *Biogeosci. Discuss.* **2016**, 1–27. [CrossRef]
54. Lloyd, J.; Taylor, J.A. On the Temperature Dependence of Soil Respiration. *Funct. Ecol.* **1994**, *8*, 315. [CrossRef]
55. Kätterer, T.; Reichstein, M.; Andrén, O.; Lomander, A. Temperature dependence of organic matter decomposition: A critical review using literature data analyzed with different models. *Biol. Fertil. Soils* **1998**, *27*, 258–262. [CrossRef]
56. Raich, J.W.; Potter, C.S.; Bhagawati, D. Interannual variability in global soil respiration, 1980±94. *Glob. Chang. Biol.* **2002**, 800–812. [CrossRef]
57. Buysse, P.; Goffin, S.; Carnol, M.; Malchair, S.; Debacq, A.; Longdoz, B.; Aubinet, M. Short-term temperature impact on soil heterotrophic respiration in limed agricultural soil samples. *Biogeochemistry* **2013**, *112*, 441–455. [CrossRef]
58. Willey, J.M. *Prescott, Harley, and Klein's Microbiology*; McGraw-Hill: New York, NY, USA, 2008.
59. Roland, M.; Serrano-Ortiz, P.; Kowalski, A.S.; Goddéris, Y.; Sánchez-Cañete, E.P.; Ciais, P.; Domingo, F.; Cuezva, S.; Sanchez-Moral, S.; Longdoz, B.; et al. Atmospheric turbulence triggers pronounced diel pattern in karst carbonate geochemistry. *Biogeosciences* **2013**, *10*, 5009–5017. [CrossRef]
60. Sanchez-Cañete, E.P.; Serrano-Ortiz, P.; Kowalski, A.S.; Oyonarte, C.; Domingo, F. Subterranean CO_2 ventilation and its role in the net ecosystem carbon balance of a karstic shrubland. *Geophys. Res. Lett.* **2011**, *38*. [CrossRef]
61. Meyer, N.; Welp, G.; Amelung, W. The Temperature Sensitivity (Q10) of Soil Respiration: Controlling Factors and Spatial Prediction at Regional Scale Based on Environmental Soil Classes. *Glob. Biogeochem. Cycles* **2018**, *32*, 306–323. [CrossRef]
62. Kirschbaum, M.U.F. The temperature dependence of soil organic matter decomposition, and the effect of global warming on soil organic C storage. *Soil Biol. Biochem.* **1995**, *27*, 753–760. [CrossRef]
63. Mohr, M.; Laemmel, T.; Maier, M.; Schindler, D. Spatial variability of wind-induced air pressure fluctuations responsible for pressure pumping. *Tellus Ser. B Chem. Phys. Meteorol.* **2017**, *69*, 1–6. [CrossRef]
64. Laemmel, T.; Mohr, M.; Schack-Kirchner, H.; Schindler, D.; Maier, M. Direct Observation of Wind-Induced Pressure-Pumping on Gas Transport in Soil. *Soil Sci. Soc. Am. J.* **2017**, *81*, 770–774. [CrossRef]
65. Roesch, A.; Schmidbauer, H. WaveletComp: Computational Wavelet Analysis. R Package Version 1.1. 2018. Available online: https://CRAN.R-project.org/package=WaveletComp.
66. Mohr, M.; Laemmel, T.; Maier, M.; Schindler, D. Analysis of air pressure fluctuations and topsoil gas concentrations within a scots pine forest. *Atmosphere* **2016**, *7*, 125. [CrossRef]
67. Moya, M.R.; Sánchez-Cañete, E.P.; Vargas, R.; López-Ballesteros, A.; Oyonarte, C.; Kowalski, A.S.; Serrano-Ortiz, P.; Domingo, F. CO_2 Dynamics Are Strongly Influenced by Low Frequency Atmospheric Pressure Changes in Semiarid Grasslands. *J. Geophys. Res. Biogeosci.* **2019**, *124*, 902–917. [CrossRef]

68. Tillman, F.D.; Smith, J.A. Site characteristics controlling airflow in the shallow unsaturated zone in response to atmospheric pressure changes. *Environ. Eng. Sci.* **2005**, *22*, 25–37. [CrossRef]
69. Massmann, J.; Farrier, D.F. Effects of atmospheric pressures on gas transport in the vadose zone. *Water Resour. Res.* **1992**, *28*, 777–791. [CrossRef]
70. Parker, J.C. Physical Processes Affecting Natural Depletion of Volatile Chemicals in Soil and Groundwater. *Vadose Zo. J.* **2003**, *2*, 222–230. [CrossRef]
71. Kuang, X.; Jiao, J.J.; Li, H. Review on airflow in unsaturated zones induced by natural forcings. *Water Resour. Res.* **2013**, *49*, 6137–6165. [CrossRef]